9

Graphene–Semiconductor Hybrid Photocatalysts and Their Application in Solar Fuel Production

Pawan Kumar[1], Anurag Kumar[1], Chetan Joshi[1], Rabah Boukherroub[2]* and Suman L. Jain[1]*

[1]Chemical Sciences Division, CSIR-Indian Institute of Petroleum, Dehradun, India
[2]Institut d'Electronique, de Microélectronique et de Nanotechnologie (IEMN), UMR CNRS 8520, Université Lille 1, Villeneuve d'Ascq, France

Abstract

Harvesting solar light by semiconductors for conversion of carbon dioxide (CO_2) and water into fuel is a revolutionary approach for fulfilling energy appetite and mitigating increased greenhouse gases concentration in our environment. Nanocomposite materials synthesized by hybridization of semiconductors with graphenic materials owing to their better absorbance, charge separation, and higher surface area have been proved to be superior candidates for photocatalytic applications from quantum efficiency and selectivity viewpoints. This chapter is focused on the discussion of various graphene/semiconductor nanocomposite systems for enhanced photocatalytic performance for water splitting as well as CO_2 reduction. So far, extensive work has been carried out on TiO_2 and non-TiO_2 semiconductors, but still quantum efficiency is far from the real-life application and limited to 5–50 μmol. Recent developments in this realm suggested that graphene oxide (GO) or reduced GO boosted the performance of semiconductors by facilitating charge separation. Furthermore, functionalization of these hybrids with dyes and metal complexes provided a significant enhancement in the product yield.

***Keywords*:** Semiconductors, graphene, photocatalysis, CO_2 reduction, water splitting

**Corresponding authors*: rabah.boukherroub@iemn.univ-lille1.fr; suman@iip.res.in

Ashutosh Tiwari and Mikael Syväjärvi (eds.) Advanced 2D Materials, (355–386)

9.1 Introduction

Extensive exploitation of natural resources for fulfilling energy and other materialistic demands of human being has raised the serious problem of global warming along with depletion of fossil fuel, which is the main energy source. This problem of shortage of fossil fuel and increased CO_2 concentration in environment due to burning of fossil fuel brings up the urgency to search new green alternative sources for meeting our energy demands [1–4]. As per the recent observation by Mauna Loa observatory, the concentration of CO_2 has reached up to 400 ppm in July 2015 [5, 6]. In this regard, molecular hydrogen has been suggested to be an ideal fuel because of its high energy density (140 MJ/Kg) and formation of water as only byproduct [7]. Till now, most of the hydrogen is being produced from natural gas by water reforming, which again relies on fossil fuel and produces CO_2.

Sun light is an inexhaustible and continuous source of energy and can be stored in the form of chemical bonds and electrical energy, which can fulfill hunger of energy in a very efficient way. Solar radiation reaching on the earth surface within one hour can provide energy for 1-year requirement of human being [8, 9]. In the similar way, water is the most abundant and most easily accessible resource of hydrogen. So, solar light-mediated water splitting to produce hydrogen can be a self-sustained process that relies totally on two most abundant resources. However, due to high volume to mass ratio, storage of hydrogen is difficult.

Alternatively, CO_2 can be established as an important feedstock for the production of solar fuel [10–15]. Photo-assisted chemical conversion of CO_2 to liquid fuels like formic acid, methanol and other higher hydrocarbons can be used for the storage of hydrogen in the liquid form, which in turn will reduce the increasing concentration of CO_2 in the environment [16–20]. In contrast to thermal conversion of CO_2 and hydrogen to fuel, photocatalytic conversion is a viable approach because it harvests solar energy. Due to the presence of two double bonds, CO_2 is a highly stable molecule and its one electron reduction is unfavorable due to its higher theoretical reduction potential (–1.90 V) [21–23]. Thus in a multiple proton-assisted reduction of CO_2 (Eq. 9.1–9.7), the required protons and electrons can be derived from water splitting [24–26]. So, water splitting/water oxidation and CO_2 reduction are key processes and coupling of both may provide a viable solution for sustainable production of solar fuel. The photoreduction of CO_2 will indirectly store the chemical energy of hydrogen in the form of higher hydrocarbons, which will occupy less space as well as can be easily handled due to their liquid nature, for example methanol.

$$CO_2 + 2H^+ + 2e^- \rightarrow CO + H_2O \qquad E^0 = -0.53\ V \tag{9.1}$$

$$CO_2 + 2H^+ + 2e^- \rightarrow HCOOH \qquad E^0 = -0.61\ V \tag{9.2}$$

$$CO_2 + 4H^+ + 4e^- \rightarrow HCHO + H_2O \qquad E^0 = -0.48\ V \tag{9.3}$$

$$CO_2 + 6H^+ + 6e^- \rightarrow CH_3OH + H_2O \qquad E^0 = -0.38\ V \tag{9.4}$$

$$CO_2 + 8H^+ + 8e^- \rightarrow CH_4 + 2H_2O \qquad E^0 = -0.24\ V \tag{9.5}$$

$$CO_2 + e^- \rightarrow CO_2^{-\cdot} \qquad E^0 = -1.90\ V \tag{9.6}$$

$$2H^+ + 2e^- \rightarrow H_2 \qquad E^0 = -0.41\ V \tag{9.7}$$

9.2 TiO_2-based Photocatalyst

Since the discovery of solar electrochemical water splitting by Fujishima and Honda over titanium dioxide (TiO_2), a great attention has been directed toward the production of hydrogen over various semiconductors [27, 28]. Among them, TiO_2 is the most widely studied semiconductor due to its suitable band edge positions, nontoxicity, earth abundance and stability at various pH. The reduction potential of H^+/H_2 is 0.00V at pH = 0; however, –0.41V over potential is needed for the production of hydrogen in aqueous solutions [29, 30]. So for efficient hydrogen evolution, the position of the conduction band of the semiconductor should be more negative than –0.41V. In the similar way, water oxidation potential is +1.23 V at pH = 0 or +0.82 V at pH = 7 *vs* NHE so the position of the valence band should be more positive than this value. On the other hand, the reduction potential of CO_2/CH_3OH is –0.38 V, so the photocatalyst that can reduce protons can also reduce CO_2. Conclusively, the band gap should be higher than 1.23 V for the efficient hydrogen evolution or CO_2 reduction. TiO_2 possesses a wide band gap (3.2 eV) for the anatase form and therefore can absorb only in the UV region, which represents about 5% of the total solar spectrum [31–33]. However, the visible light consists of approximately 45% of the solar spectrum. Therefore, for efficient utilization of solar energy, the photocatalyst should be able to absorb in the visible region, which means that the band gap should be small. Hence, these two conditions are contradictory, *i.e.,* for efficient reduction of protons and CO_2, and water oxidation the band gap should be higher, whereas for absorbing the visible light in solar spectrum the band gap should be smaller. As the conduction band of TiO_2 and other semiconductors is slightly negative than the reduction potential of CO_2 or protons so lowering the position of conduction band will compromise the CO_2 or water reduction capacity. The valence band position of TiO_2 is +2.53 V *vs* SHE so the valence band can be shifted upward by band gap engineering [34, 35]. In this direction, doping with non-metals

like C [36–38] and N [39–41] has been proved to be effective. For example, when TiO_2 was doped with nitrogen, the 2p orbital of nitrogen having higher energy overlapped with O 2p orbital of TiO_2 so the position of the valence band was shifted upward, enhancing the absorption profile of TiO_2 in the visible region [42, 43]. However due to fast electron–hole pair recombination, the quantum efficiency of these systems remained too far from practical utilization. Electron–hole pair recombination can be divided into two main categories: the first one is volume recombination and the second one is surface recombination [44]. In the volume recombination, the photogenerated electron–hole pairs recombine before reaching the surface of catalyst, so they cannot take part in the reduction or oxidation processes. The volume recombination can be minimized by reducing the size of the photocatalyst to nanometer range so electrons and holes can move on the surface and can reduce or oxidize adsorbed substrates [45–47]. In the surface recombination, the electrons and holes recombine at the interface of catalyst; this recombination can be prevented by doping with electron and hole capturing agents. Electron capturing agents also called co-catalysts consist of metals such as Co [48–50], Ru [51, 52], Cu [53–55], and Au [56, 57], which possess the Fermi levels just below the conduction band so electrons can rapidly move to metal and better charge separation can be achieved. Hole capturing agents or scavengers are mainly metal oxides like IrO_2 [58–60]. In general, semiconductor photocatalysts provide hydrocarbon products having lower C:H ratio because of cessation of reaction on the surface of catalyst. So, in order to produce hydrocarbons with higher C:H ratio, multi-electron transfer is essential. Modification of semiconductors with certain dopants can fulfill the criterion of multi-electron transfer. The multi-electron transfer is possible by sensitization of semiconductors with molecular catalysts, which have the ability to generate more than one electron–hole pair simultaneously [61, 62].

9.3 Non-TiO_2 Semiconductors

Semiconductors other than TiO_2 such as ZnO [63–65], ZnS [66], $InTaO_4$ [67], $ZnGa_2O_4$ [68], CdS [69, 70], $InVO_4$ [71], and WO_3 [72] have been widely explored for hydrogen evolution reaction as well CO_2 reduction. Mixed metal oxides like $Ru_xTi_{1-x}O_2$ [73], Rh–Cr mixed oxide nanoparticles, dispersed $(Ga_{1-x}Zn_x)N_{1-x}O_x$ [74], and ZrO_2-supported $Ni_xFe_{3-x}O_4$ [75] have been proven to be better photocatalysts than single metal oxides. Adding a low-band-gap semiconductor to high-band-gap semiconductor is advantageous because it increases the lifetime of excited state indirectly by continuous pumping of electrons in the conduction band and transferring holes in the valence band [76, 77]. According to the mechanism in such systems, the electrons and holes generated on the low-band-gap semiconductor are transferred to

high-band-gap semiconductor where reduction and oxidation reactions take place. Except in some cases, most of the semiconductors have such band position that they can only support either oxidation (positive VB but less negative CB) or reduction (negative CB but less positive VB). However, for sustaining the continuous generation of hydrogen or CO_2 reduction both reactions should take place simultaneously. Thus, making a composite material by combining two semiconductors in which one can initiate reduction reaction and other can sustain oxidation reaction may provide a viable solution to overcome this problem. These types of composite work by following the Z-scheme mechanism (Figure 9.1), in which two semiconductors behave like p–n heterojunction [78–80]. The semiconductor having more positive valence band absorbs visible light and generates electron–hole pairs. The holes are used for the oxidation of water while the photogenerated electrons are transferred to the valence band of the other semiconductor that has a negative conduction band. Then the electrons in the valence band can move to the conduction band after absorption of light and can be used for the reduction of protons or CO_2. So, the Z-scheme photocatalysts work on a two-step photo-excitation process (Figure 9.1). For example, Z-scheme photosystem composed of Pt/$SrTiO_3$:Rh as hydrogen evolving catalyst and $BiVO_4$ as oxygen evolving catalyst was visible light responsive in the presence of Fe^{3+}/Fe^{2+} redox couple and can operate under 520 nm wavelength, which corresponds to the band gap of $SrTiO_3$:Rh and $BiVO_4$ [81].

9.4 Metal Complexes Sensitized Semiconductors

Apart from doping and mixing semiconductors, sensitization is also a promising approach for enhancing the visible-light performance of semiconductor

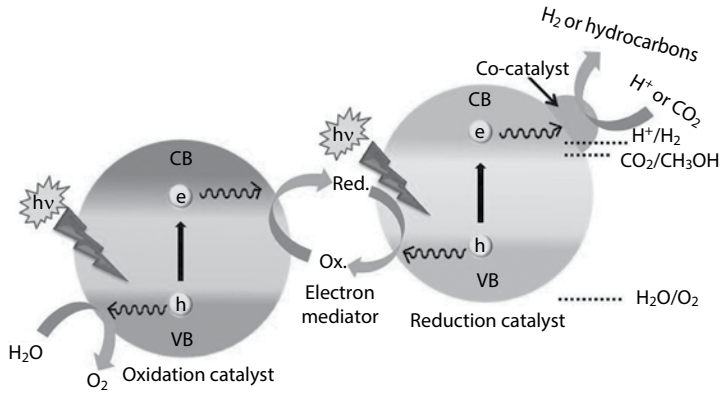

Figure 9.1 Mechanism of Z-scheme photocatalyst for hydrogen evolution or CO_2 reduction.

materials. Homogeneous metal complexes like bipyridyl complexes of ruthenium, iridium, cobalt, metal phthalocyanines, organic dyes, etc. have been found to be the best sensitizing materials for improving visible-light absorption performance [82]. The metal complexes after absorption of visible light are excited by MLCT (metal-to-ligand charge transfer) transition and electrons are transferred from HOMO to LUMO. The excited species was able to transfer electrons to the conduction band of a semiconductor. For example, in a recent report, Kumar *et al*. demonstrated that Ru complex and cobalt phthalocyanine binuclear complex grafted on magnetically separable TiO_2 can efficiently reduce CO_2 to methanol [83]. The methanol formation rate by using Ru-CoPc@TiO_2@SiO_2@Fe_3O_4 catalyst was found to be 53.5 μmol g^{-1} h^{-1} after 48 h. The particular combination of metal complexes was chosen because the lifetime of the ruthenium complex was shorter (~0.385–0.421 μs) in comparison to CoPc (~170–245 μs) so it can transfer electrons to the CoPc [84]. For efficient electron injection in the conduction band of the semiconductor, a longer lifetime is required, so CoPc can efficiently transfer electrons to the conduction band of TiO_2. Although the sensitization of semiconductor photocatalysts with metal complexes increases the quantum efficiency, the high cost and leaching of metal complexes from the surface of the semiconductor are the major drawbacks. To overcome these limitations, *in situ* synthesis of metal complex grafted semiconductor composite materials has proved to be more promising. In this regard, Kumar *et al*. demonstrated that *in situ* synthesized $Ru(bpy)_3Cl_2/TiO_2$ nanocomposite to be an efficient heterogeneous photocatalyst for photoreduction of CO_2 to methanol [85]. The *in situ* synthesized $Ru(bpy)_3Cl_2/TiO_2$ nanocomposite gave selectively methanol in the presence of triethylamine as a sacrificial donor with a formation rate of 78.1 μmol g^{-1} h^{-1} and a quantum yield of 0.24 mol $Einstein^{-1}$. The quantum yield at different wavelengths followed the absorption pattern of the ruthenium complex, which clearly depicted that ruthenium complex played a pivotal role in charge transfer by absorption of visible light (Figure 9.2I). The origin of enhanced photocatalytic performance was attributed to better electron injection in the conduction band of TiO_2 (Figure 9.2II).

9.5 Graphene/Semicondutor/Metal Complexes-based Photocatalyst

Since its discovery by Geim and Novoselov, graphene, a two-dimensional sp^2 carbon material has attracted a tremendous attention of the scientific community due to its exceptional properties [86]. Graphene is an allotrope of carbon, composed of layers of sp^2-hybridized carbon atoms packed into a honeycomb network. Due to the 2D network of conjugated carbon, graphene possesses

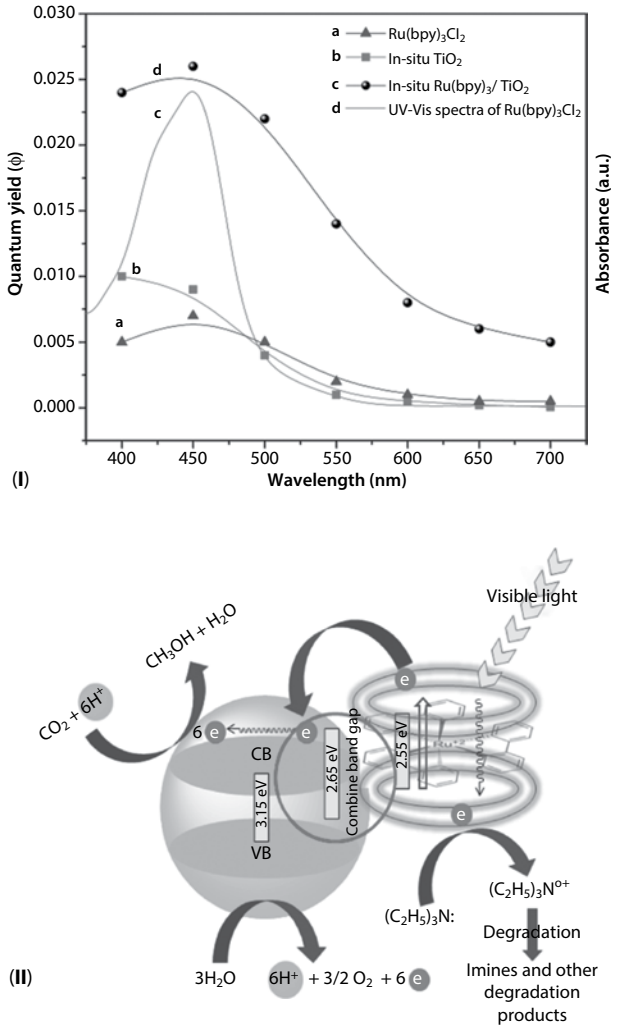

Figure 9.2 (I) Quantum yield of methanol at different wavelengths by using a) $Ru(bpy)_3Cl_2$, b) *in situ* TiO_2, c) *in situ* $Ru(bpy)_3/TiO_2$, and d) UV–Vis spectrum of $Ru(bpy)_3Cl_2$. (II) Plausible mechanism of CO_2 photoreduction using the *in situ* $Ru(bpy)_3/TiO_2$ nanocomposite. Reproduced from Ref. 85 with permission from The Royal Society of Chemistry.

specific properties like high mobility of charge carriers (>200 000 $cm^2 V^{-1} s^{-1}$), exceptional Young's modulus values (~1.0 TPa), large spring constants (1–5 Nm^{-1}), theoretically high specific surface area (2630 $m^2 g^{-1}$), excellent thermal conductivity (~5000 W $m^{-1} K^{-1}$), and optical transmittance (~97.7%) [87]. Owing to these fascinating properties, graphene has been widely investigated for different applications like nanoelectronics, optoelectronics, chemical and biochemical sensing, polymer composites, organic transformations, hydrogen

evolution, CO_2 reduction, dye degradation, VOCs (volatile organic chemicals) degradation, energy storage, drug delivery, supercapacitors, catalysis, photovoltaics, etc. [88–94]. Among the various applications, photocatalytic water splitting and CO_2 reduction are of particular importance because of alarming condition in decrease of fossil fuel and rising concentration of greenhouse gases. Graphene due to its zero band gap cannot participate in charge separation step of photocatalysis. However, because of its higher electron mobility and high specific surface area, it can assist in better charge separation on its interface. Various nanocomposite materials of graphene with semiconductors, metal complexes, dyes, etc. have shown excellent performance for the photo-induced water splitting and CO_2 reduction [95–97]. In the graphene semiconductor composite, the semiconductor after absorption of light generates electron–hole pairs and graphene provides mobility to the electrons. Furthermore, graphene improves the visible-light absorption performance of semiconductor *via* synergistic effect (Figure 9.3).

Recently, many graphene-based nanohybrid composites have been synthesized with various semiconductors like TiO_2 [98, 99], ZnO [100, 101], WO_3 [102], Cu_2O [103], Fe_2O_3 [104], MnO_2 [105], ZrO_2 [106], ZnS [107], CdS [108], CdSe [109], Bi_2WO_6 [110], $BiVO_4$ [111], $Sr_2Ta_2O_7$ [112], $InVO_4$ [113], $ZnFe_2O_4$ [114], etc. by following two main synthetic strategies. The first approach involves mixing of graphene with the semiconductor in a suitable solvent (solution mixing method), while the second approach relies on mixing of the precursor salt of the semiconductor and graphene oxide (GO) at a suitable pH (*in situ* growth method). In contrast to graphene, which has zero band gap and behaves like a conductor, GO behaves like a semiconductor and possesses a band gap [115]. Harsh oxidation of graphite to produce GO adds oxygen containing functional groups at the

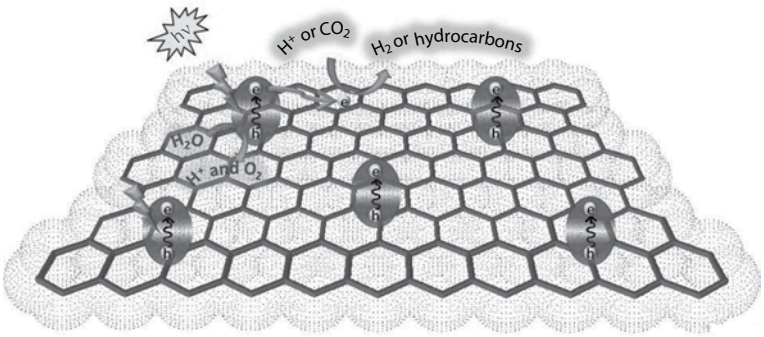

Figure 9.3 Mechanism of hydrogen evolution or CO_2 reduction on the surface of graphene/semiconductor composite.

basal planes as well on the edges, which transforms most of the sp^2 carbons into sp^3 carbons. Thus, enormous domains of sp^2 and sp^3 oxidized carbons are evolved on the surface of GO. The sp^2 carbons, due to extensive conjugation, facilitate electron movement in these domains without any resistance and behave like a conduction band, while sp^3 carbons due to localized electrons prevent free electron movement and behave like a valence band. So, a band gap is created due to the presence of sp^2- and sp^3-hybridized carbons and the value of this band gap strongly depends on the degree of GO oxidation [116]. In a recent study by Hsu *et al.*, the band gap value of as-synthesized graphene oxide (GO-3) by oxidation of graphite with H_3PO_4 and H_2SO_4 was found to be in the range of 2.9–3.7 eV due to the uneven oxidation of graphene sheets. The conduction band position of GO-3 was negative enough (–0.79 V *vs* NHE) to facilitate CO_2 reduction to methanol while the position of the valence band (+2.91 V *vs* NHE) was positive enough to perform water splitting. In this study, CO_2 to methanol formation rate (R_{MeOH}) was 0.172 μmol g cat^{-1} h^{-1} by using GO-3 [117]. A similar report by Yeh *et al.* showed that highly oxidized GO can serve as a good photocatalyst for the hydrogen evolution from water [118]. In the GO, the conduction band which is composed of antibonding π^* orbital has higher energy than the reduction potential required for hydrogen generation. By using GO and water alone, the yield of hydrogen was 280 μmol after 6 h of visible irradiation. However, addition of platinum as a co-catalyst and methanol as a sacrificial donor enhanced the yield up to 17000 μmol after 6 h. The increased yield was ascribed to methanol, which acts as a hole scavenger and inhibits electron–hole recombination.

Similarly the addition of hole capturing agents like metals on GO can improve its photocatalytic efficiency. In this regard, GO decorated with copper nanoparticles of 4–5 nm in diameter exhibited improved photocatalytic performance due to diminished charge recombination rates [119]. Furthermore, the effect of copper loading was investigated and it was found that 10 wt.% Cu NPs loaded on GO (Cu/GO-2) gave the highest rate of methanol production (2.94 μmol g^{-1} h^{-1}) after 2 h irradiation with 3.88 μmol g^{-1} h^{-1} of acetaldehyde. In the proposed mechanism, it has been suggested that after absorption of visible light, the photogenerated electrons were captured by Cu metal and then efficient transfer of electrons from Cu d orbital to C–O π^* orbital initiated multi-electron transfer to yield methanol and acetaldehyde. In a study by Xu *et al.*, it has been demonstrated that partially reduced graphene oxide (PRGO) acts as a p-type semiconductor which can create a p–n heterojunction with CPNP (coordination polymer nanoplates) $[Cu(pad)_2(bipy)]_n \cdot n(H_2pad)$ (CP) (pad=phenylenediacrylate dianion, bipy=4,4′-methyl-2,2′-bipyridine) in

PRGO/CPNP photocatalyst [120]. It was found that the reductive degree of the PRGO had a great influence of the H_2 production rate. Among the various PRGO/CPNP hybrids studied, the highest H_2 production rate achieved was 33.75 μmol h^{-1}.

It has previously been shown that doping of semiconductors with non-metals can alter the energy levels of the valence band by hybridization and thus reduces the band gap of the semiconductor for absorption in the visible region [121]. However, faster recombination of photogenerated charges prevents from achieving the goal of higher quantum efficiency. Hybridization of doped semiconductors with GO can overcome this problem of charge neutralization. In addition, due to the presence of a band gap, GO can work synergistically for better electron and hole separation by making p–n heterojunction.

Earlier in 2012, Pie *et al*. have prepared nitrogen-doped TiO_2/GO nanocomposite (NTG) for better photoactivity for visible-light-mediated hydrogen evolution [122]. Nitrogen-doped TiO_2 had already been investigated by researchers and regarded as a promising photocatalyst for hydrogen evolution under visible light. TiO_2 hybridization with GO not only narrows its band gap for visible-light absorption, but also delays the electron–hole recombination rate, which enhances its photocatalytic efficiency. Under visible-light irradiation, the photogenerated electrons are transferred from the conduction band of NT (nitrogen-doped TiO_2) to GO which not only acts as an electron trapper but also accelerates the process of electron transfer to the target molecule due to the higher mobility of electrons and prevents the photo-generated electrons from coming back to the valence band of TiO_2 or N 2p level of NT. Introduction of GO to *N*-TiO_2 enhances the photocatalytic efficiency by 13.6 times as compared to commercially available P25, yielding 112.0 μmol g^{-1} h^{-1} hydrogen.

Very recently, Tan *et al*. reported a promising GO-doped oxygen rich TiO_2 (GO–OTiO_2) binary nanocomposite, prepared *via* a highly convenient wet chemical impregnation technique, as efficient photocatalyst for the photoreduction of CO_2 to CH_4 in the presence of water vapor [123]. The reaction was carried out under very mild conditions like using day light bulb as a source of visible light. The oxygen rich TiO_2 was prepared by precipitation of titanium butoxide in cold water using hydrogen peroxide as an oxidant. The enhanced activity of oxygen-rich TiO_2 for the CO_2 photoreduction was attributed to the narrowing of the band gap to 2.95 eV and incorporation of oxygen defects served as electron scavengers so the lifetime of the photogenerated carriers was increased [124]. However, the photoactivity of O_2–TiO_2 catalyst, i.e., the yield of CH_4 gradually decreases over time after reaching a maximum value. Such unusual behavior was also reported earlier by Liu *et*

al. [125] and Wang *et al.* [126] where the activity of photocatalyst decreased after reaching its maximum value. The reason for such uncommon behavior could be due to the retention of maximum adsorption sites and fast electron–hole recombination rates. Therefore, to overcome this drawback, O_2–TiO_2 hybrid was incorporated with GO sheets, which significantly increases its photoactivity as well as reduces electron–hole recombination. The formation rates of CH_4 over O_2–TiO_2 and GO–OTiO_2 nanocomposite were 1.026 and 1.718 μmol g^{-1} cat after 6 h, respectively. GO plays an indispensable role in increasing the lifetime of charge carriers required for the reduction of CO_2. The optimal content of GO was investigated and found to be 5 wt.% with respect to O_2–TiO_2 giving the highest yield of CH_4. Further increase in the GO amount leads to a decrease in the photoactivity of the nanocomposite, which may be due to the unavailability of visible-light adsorption sites on O_2–TiO_2 due to high carbon content. GO–OTiO_2 nanocomposite gave 14 folds higher yield as compared to commercially available Degussa P25. The prominent role of GO can be explained on the basis of interaction between d-orbital of O_2–TiO_2 and π-orbital of GO which forms d–π orbital overlapping, leading to formation of strong chemical interaction among the two; this favors electron–hole charge separation by hampering the charge recombination, which subsequently enhances the visible-light efficiency and the yield of the desired product.

Due to the presence of a suitable band gap and various functional groups, GO provides an opportunity for covalent attachment of homogeneous metal complexes [127, 128]. As metal complexes have good visible-light absorption, they can work as photosensitizers. Immobilization approach not only improves the visible-light absorption efficiency but also makes the recovery of expensive metal catalysts feasible. In this regard, ruthenium polyazine macromolecular complex [129] and cobalt phthalocyanine [130] have been successfully immobilized on GO for the photoreduction of CO_2 to methanol with the formation rates of 82.8 and 78.8 μmol g^{-1} h^{-1}, respectively, in the presence of triethylamine as a sacrificial donor. To make the developed methodology more promising, it is essential to remove the need of a sacrificial donor. Synergistic mechanism can play an efficient role: metal complexes generate electrons and transfer them to the conduction band of the semiconductor, while positive charges of the metal complexes move to the valence band of the semiconductor, so indirectly electron–hole pairs are generated in the conduction and valence bands of the semiconductor. Very recently Kumar *et al.* have synthesized a new heteroleptic ruthenium complex bearing 2-thiophenylbenzimidazole ligand and subsequently immobilized it on GO (Figure 9.4) [131]. Along with –OH and –COOH groups, epoxide functionalities located on the basal

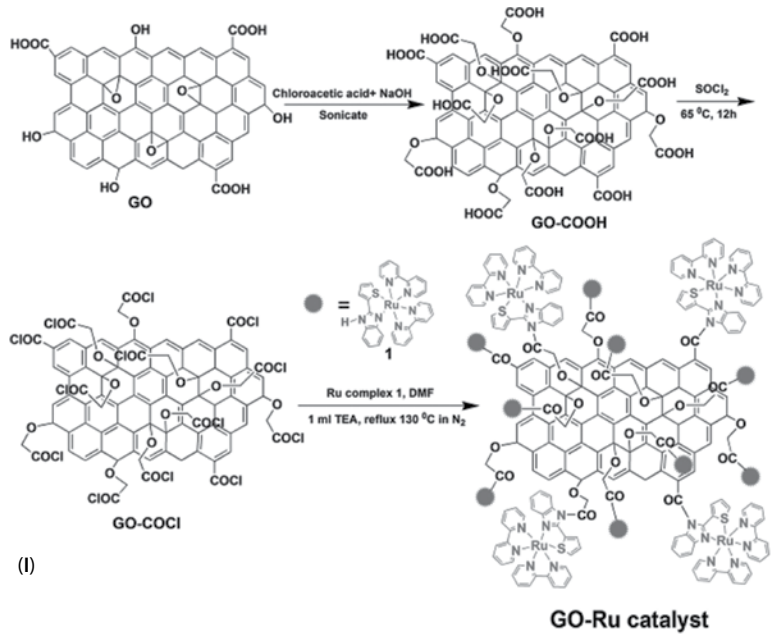

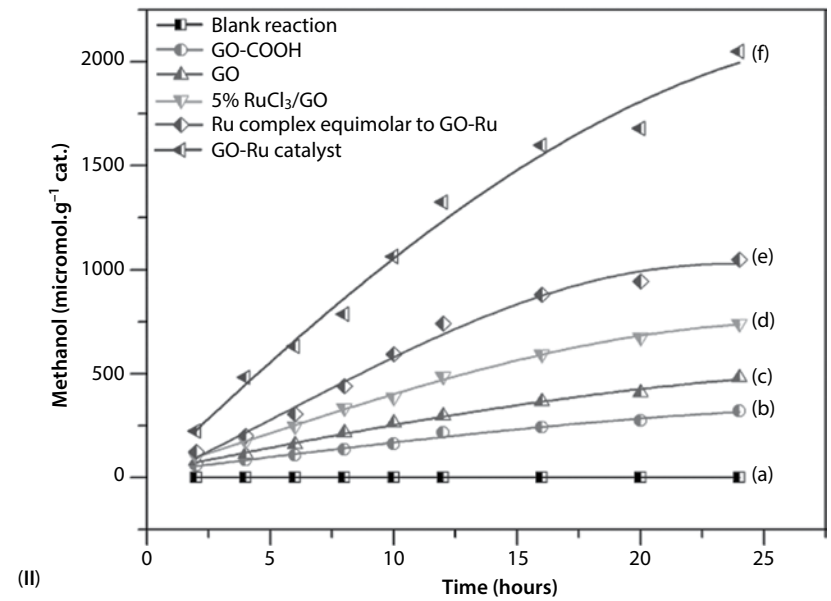

Figure 9.4 (I) Synthetic scheme of GO–Ru catalyst and (II) CO_2 to methanol yield: (a) blank reaction, using (b) GO–COOH, (c) GO, (d) 5% $RuCl_3$/GO, (e) Ru complex equimolar amount to GO–Ru catalyst, and f) GO–Ru catalyst. Reproduced from Ref. 131 with permission from The Royal Society of Chemistry.

plane of GO sheets were used for the functionalization to reach a higher loading of the complex on the GO support (Figure 9.4I). The synthesized GO–Ru photocatalyst exhibited superior catalytic activity for the visible-light-induced reduction of CO_2 to methanol. Methanol was selectively formed during the catalytic step with a formation rate of 85.4 μmol g^{-1} cat after 24 h and associated quantum yield (ϕ) of 0.09 (Figure 9.4II). The covalent attachment of the Ru complex to the surface of GO made the catalyst robust and leach proof. Recycling experiments depicted that there was no loss in catalytic activity even after three recycling experiments. The enhanced photoactivity after immobilization of the Ru complex on GO was due to better charge injection from MLCT excited Ru complex to the conduction band of GO (Figure 9.5). Importantly, the developed catalytic system did not require any sacrificial donor and can extract required electrons and protons through water splitting due to the more positive oxidation potential of GO than water.

Hybridization of metal clusters/metal organic frameworks (MOF)/polyoxometallate (POM) with graphene or GO has proved to enhance the catalytic performance *via* synergistic effect of better charge separation or efficient electron transfer in the conduction band of GO. Metal clusters of Mo and Re can selectively produce hydrocarbons with high C:H ratio due to the presence of multi-metallic centers, which can transfer multiple electrons required for producing higher hydrocarbon products [132]. In this context, octahedral hexamolybdenum clusters have recently been used for selective methanol formation from CO_2 photoreduction. However, the homogeneous nature and requirement of sacrificial agents limit their

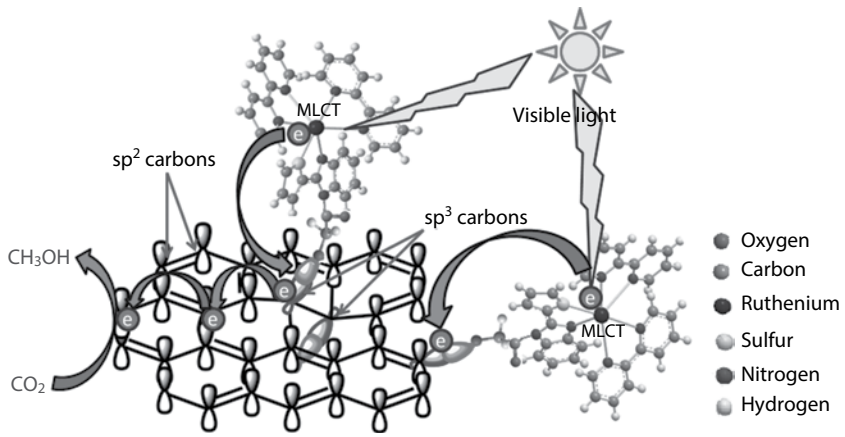

Figure 9.5 Plausible mechanism of CO_2 photoreduction to methanol catalyzed by GO–Ru. Reproduced from Ref. 131 with permission from The Royal Society of Chemistry.

practical application. Immobilization of the metal clusters on photoactive supports can solve both issues by making them recyclable as well as oxidizing water for deriving required electrons and protons. Consequently, Kumar *et al*. have prepared heterogenized octahedral Mo clusters having Cs and TBA (tetrabutylammonium) counter ions/GO by taking advantage of labile nature of apical halogens atoms [133]. During immobilization, apical bromine atoms were replaced by various oxygen containing functionalities present on the GO (Figure 9.6). The chemical nature of immobilized metal clusters on GO support was confirmed by X-ray photoelectron spectroscopy (XPS) analysis. The XPS analysis of metal clusters ($Cs_2Mo_6Br^i_8Br^a_6$/$(TBA)_2Mo_6Br^i_8Br^a_6$) and their composite with GO (GO–$Cs_2Mo_6Br^i_8Br^a_x$ and GO–$(TBA)_2Mo_6Br^i_8Br^a_x$) showed that the intensity of 3d peak component due to apical bromine atoms was reduced significantly, while peaks due to Mo 3d and Cs 3d did not change, suggesting that apical bromine atoms were replaced during immobilization (Figure 9.7).

The developed GO–$Cs_2Mo_6Br^i_8Br^a_x$ and GO–$(TBA)_2Mo_6Br^i_8Br^a_x$ photocatalysts gave methanol selectively from CO_2 with a formation rate of 68.5 and 53.9 μmol g^{-1} h^{-1}, respectively, after 24 h irradiation using 20 W LED spotlight as visible-light source (Figure 9.8). The quantum yield and turn over number by using GO–$Cs_2Mo_6Br^i_8Br^a_x$ were determined to be 0.015 and 19.0, respectively, while for GO–$(TBA)_2Mo_6Br^i_8Br^a_x$ the obtained values were 0.011 and 10.38, respectively. These values were significantly higher than those obtained by using either GO or homogeneous clusters as catalysts. Furthermore, the heterogeneous nature of the GO-supported catalyst provides facile recovery and recycling ability for several runs without losing its catalytic performance. In order to gain a better understanding on the enhanced photocatalytic performance, the band gap of GO–$Cs_2Mo_6Br^i_8Br^a_x$ and GO–$(TBA)_2Mo_6Br^i_8Br^a_x$ composites was determined and found to be 0.9 and 1.5 eV, respectively, due

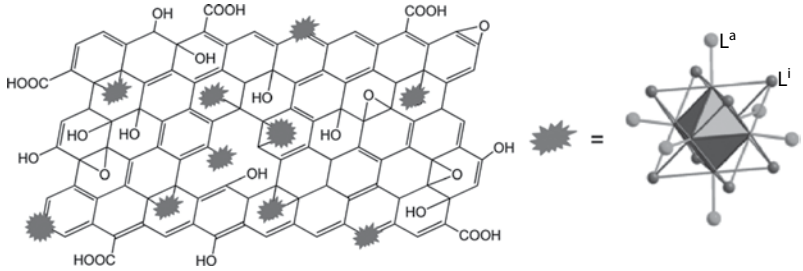

Figure 9.6 Schematic illustration of $Cs_2Mo_6Br^i_8Br^a_6$/$(TBA)_2Mo_6Br^i_8Br^a_6$ clusters immobilized on GO nanosheets and molecular structure of Mo_6 cluster representing the position of inner (L^i) and apical (L^a) ligands. Reproduced from Ref. 133 with permission from Elsevier.

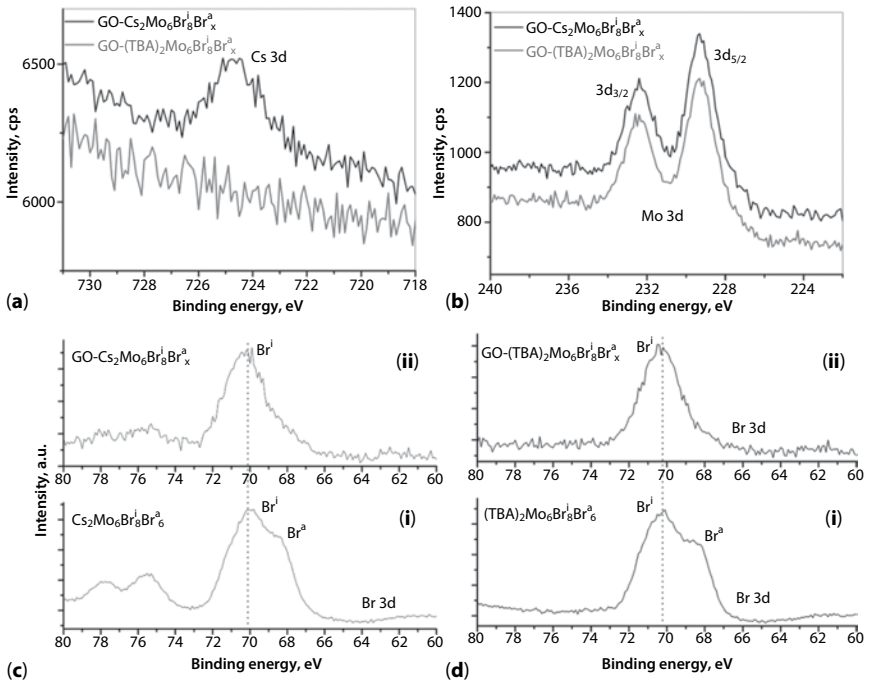

Figure 9.7 XPS spectra of (a) Cs 3d, (b) Mo 3d, (c) Br 3d regions for $Cs_2Mo_6Br^i_8Br^a_x$ and GO–$Cs_2Mo_6Br^i_8Br^a_x$, (d) Br 3d regions for $(TBA)_2Mo_6Br^i_8Br^a_x$, and GO–$(TBA)_2Mo_6Br^i_8Br^a_x$ composites. Reproduced from Ref. 133 with permission from Elsevier.

to mixed transition of Mo clusters and GO. A plausible mechanism was proposed in which metal clusters after absorption of visible light are excited and generate Mo_6* excited state. The excited Mo_6* clusters can transfer multiple electrons to the conduction band of GO. Because the position of GO conduction band is more negative than the reduction potential of CO_2/CH_3OH (–0.38 V *vs* NHE at pH 7), it can efficiently reduce CO_2 to methanol. While the valence band position is more positive than the oxidation potential of water, so it can oxidize water producing electrons and protons which can be used for the reduction of CO_2 (Figure 9.9).

Gusain *et al.* have synthesized CuO nanorods of different breadths by precipitation in aqueous solution of NaOH. The nanorods were further functionalized with APTMS (aminopropyl trimethoxysilane) to make them positively charged. Finally, mixing the positively charged nanorods with negatively charged GO solution followed by reduction gave rGO–CuO nanocomposites [134]. The breadth of CuO nanorods was found to be dependent on the concentration of NaOH and named after the ratio of

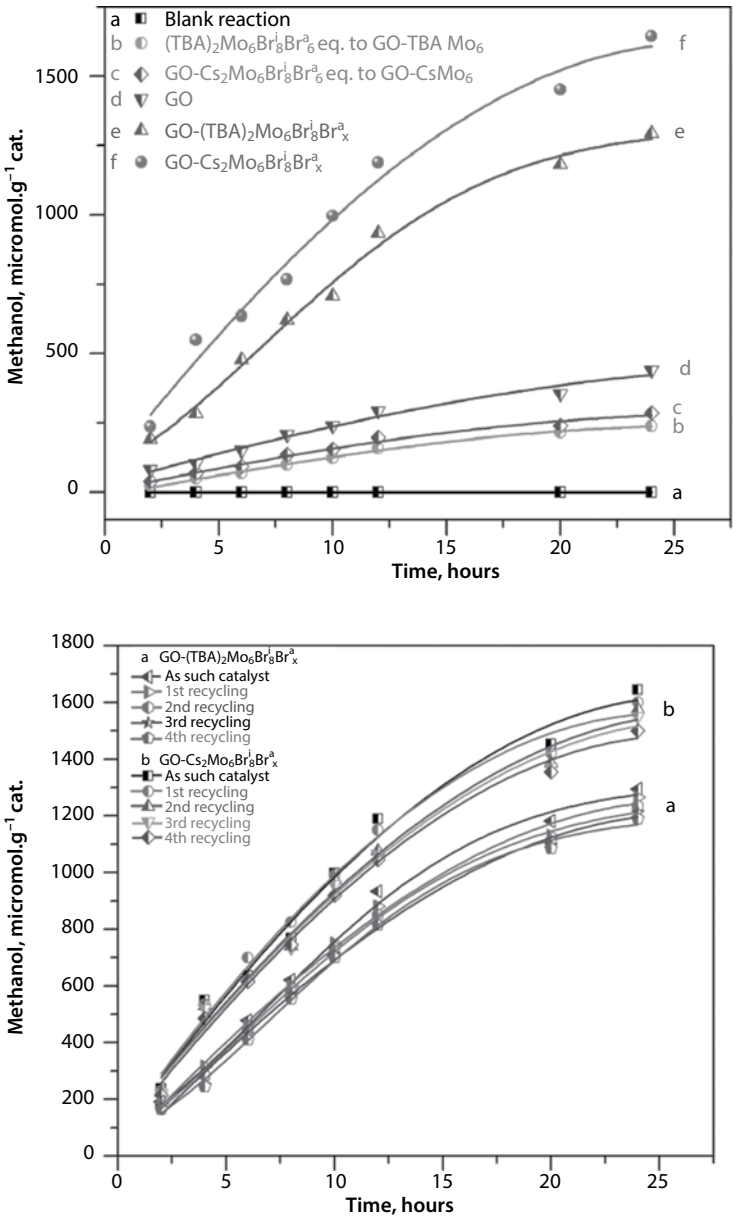

Figure 9.8 Methanol yield for a) blank reaction, b) $(TBA)_2Mo_6Br^i_8Br^a_6$ equimolar amount present in GO–$(TBA)_2Mo_6Br^i_8Br^a_x$, c) $Cs_2Mo_6Br^i_8Br^a_6$ equimolar present in GO–$(TBA)_2Mo_6Br^i_8Br^a_x$, d) GO, (e) GO–$(TBA)_2Mo_6Br^i_8Br^a_x$, and f) GO–$Cs_2Mo_6Br^i_8Br^a_x$ photocatalyzed reactions and recycling experiments using a) GO–$(TBA)_2Mo_6Br^i_8Br^a_x$ and b) GO–$Cs_2Mo_6Br^i_8Br^a_x$. Reproduced from Ref. 133 with permission from Elsevier.

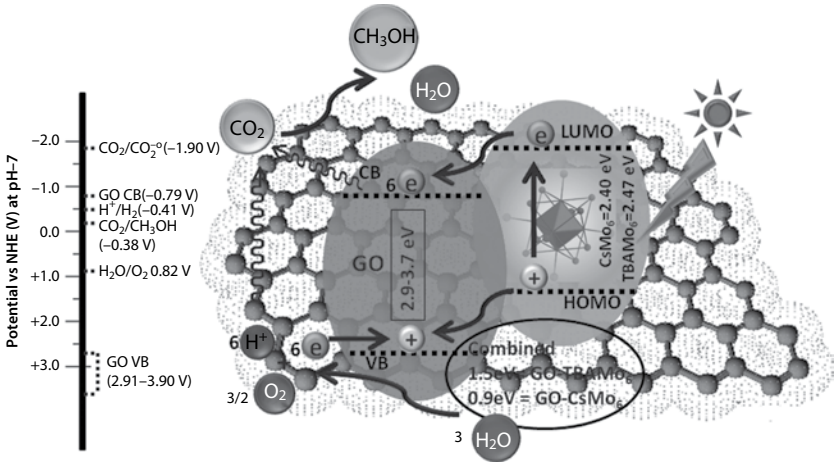

Figure 9.9 Plausible mechanism of CO_2 photoreduction into methanol catalyzed by GO–hexamolybdenum composite. Reproduced from Ref. 133 with permission from Elsevier.

NaOH to copper salt. The breath of CuO nanorods increased by increasing the molar ratio of copper salt to NaOH from 1:4 to 1:24, and was found to be 3–6, 5–9, 9–11, and 10–15 nm for rGO–CuO_{14}, rGO–CuO_{18}, rGO–CuO_{116}, and rGO–CuO_{124} nanocomposites, respectively (Figure 9.10I). The rGO–CuO nanocomposites were used for the photocatalytic reduction of CO_2, and in all cases, methanol was formed as the major product without the need of any sacrificial donor. The highest rate of methanol was obtained using rGO–CuO_{116} composite with a formation rate (R_{MeOH}) of 51.1 μmol g^{-1} h^{-1} after 24 h (Figure 9.10II and III).

In another approach, Zhang *et al.* synthesized ZnO–rGO nanocomposite *via* a simple one-step hydrothermal process and investigated its photocatalytic activity for reduction of CO_2 to CH_3OH [135]. The optical properties of the synthesized hybrid material were examined using UV–Vis diffuse reflectance spectra (DRS), which depicted the absorption of ZnO nanocrystals in the UV spectrum of light, while ZnO–rGO exhibited visible-light absorption. Graphene plays a significant role by extending the optical absorption of ZnO to higher wavelengths. It is expected to favor electron–hole separation and to decrease the recombination rate at the interface of the semiconductor. It further traps the photogenerated electrons transferred from the conduction band of ZnO, under visible-light irradiation, and utilizes them for the reduction of CO_2 adsorbed on its surface. Simultaneously, holes were created on the surface of ZnO leading to water splitting into O_2 and H^+ ions. The optimum content of GO was found

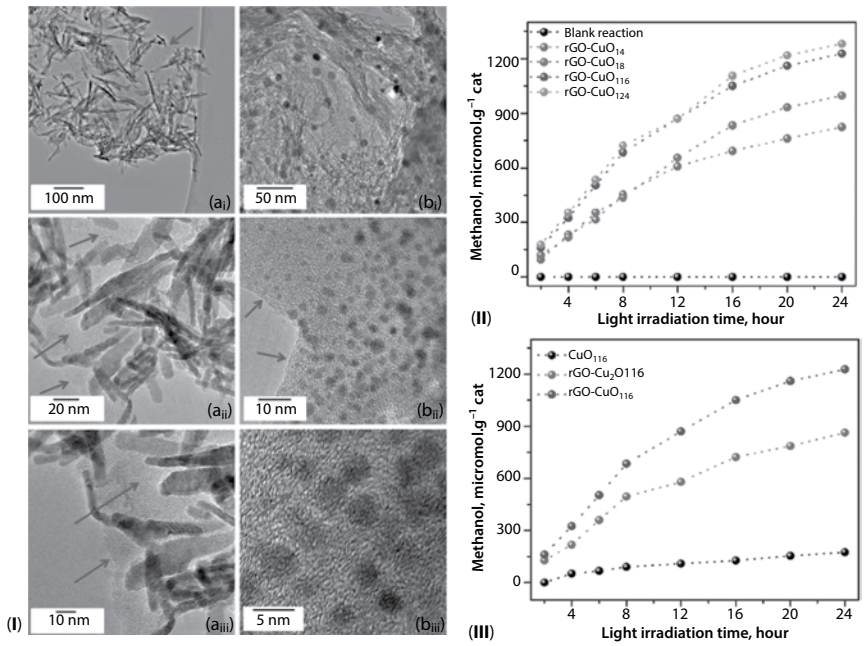

Figure 9.10 (I) HRTEM images of (a_i–a_{iii}) rGO–CuO_{116} and (b_i–b_{iii}) rGO–Cu_2O_{116} nanocomposites. (II) Methanol yield by photocatalysis of CO_2 as a function of visible-light irradiation time using rGO–CuO as photocatalyst. (III) Methanol yield by photocatalysis of CO_2 as a function of light irradiation time using CuO_{116}, rGO–Cu_2O_{116}, and rGO–CuO_{116} nanocomposites as photocatalysts. Reproduced from Ref. 134 with permission from Elsevier.

to be 10% and a maximum yield of 263.17 μmol g^{-1} cat for methanol was obtained after 3 h of visible-light irradiation.

MoS_2/RGO nanocomposite synthesized by a single-step hydrothermal method by using $(NH_4)_2MoS_2$ and GO as precursors of MoS_2 nanoparticles and reduced graphene oxide (RGO), respectively, was found to give higher photo-electrochemical performance for hydrogen evolution reaction [136]. The higher activity was attributed to the nanoscopic few layered MoS_2 with an abundance of exposed edges stacked onto graphene. According to the report of Xiang *et al.*, TiO_2 grown on MoS_2/graphene hybrid further enhanced the rate of hydrogen production [137]. Comparing with the binary nanocomposite of MoS_2/TiO_2 and TiO_2/graphene, ternary TiO_2/MoS_2/graphene composite exhibited higher photocatalytic performance and higher H_2 production rate by four and five times, respectively. The hydrogen production rate was 165.3 μmol h^{-1} by using 0.5 wt.% MoS_2/graphene co-catalyst having graphene content of 5.0 wt.% at 365 nm in the presence of ethanol as a sacrificial donor.

Ternary hybrid materials for example CdS/metal Oxide/GO–metal oxide (ZnO, Al_2O_3) have been synthesized by a two-step method. Firstly, CdS/metal oxide heterostructure was prepared by one pot hydrothermal method followed by blending of GO to the semiconductor heterostructure by simple solid state mixing [138]. The synthesized catalyst was found to be very active for the visible-light-mediated hydrogen evolution and dye degradation. It was found that the catalyst having ZnO as metal oxide was more active in comparison to Al_2O_3. This increased activity can be attributed to the CB of CdS (–0.88 eV) which is in close proximity with the CB of ZnO (–0.22 eV), so electrons can be transferred to CB of ZnO. Hole scavengers like Na_2S and Na_2SO_3 were essential for higher formation rate of hydrogen and degradation of dye.

Tan *et al*. have investigated the doping of noble metals (Pt, Pd, Au, Ag) on rGO/TiO_2 hybrid [139]. rGO/TiO_2 nanocomposite was synthesized using hydrothermal method followed by doping of Pt particles over rGO/TiO_2 nanocomposite *via* simple polyol process. The Pt-modified rGO/TiO_2 nanocomposite exhibited enhanced photocatalytic activity towards reduction of CO_2 under visible-light irradiation. Comparing all the metal-doped rGO/TiO_2 nanocomposites, Pt-GT (Pt-doped rGO/TiO_2) nanocomposite exhibited higher photoactivity (1.696 μmol g^{-1} CH_4) in comparison to other metal-doped rGO/TiO_2, i.e., Pd–GT (1.193 μmol g^{-1} CH_4), Ag–GT (0.998 μmol g^{-1} CH_4), Au–GT (0.756 μmol g^{-1} CH_4), and GT (0.651 μmol g^{-1} CH_4). Pt-doped rGO/TiO_2 hybrid displayed 2.6 and 13.2 folds higher activity than blank TiO_2 (0.126 μmol g^{-1} CH_4) and commercially available P25 (0.129 μmol g^{-1} CH_4), respectively, after 6 h of light irradiation. The synergistic effect, where graphene sheets act as an electron trapper and transporter of photogenerated electron–hole pairs, enhanced the photoactivity of rGO/TiO_2 nanocomposite. Furthermore, the Pt nanoparticles on the surface of rGO/TiO_2 efficiently trap the photogenerated electrons for reduction of CO_2.

Owing to the growing economical considerations, efforts have been made to develop noble metal free photocatalysts by using graphene as a substitute for noble metal on semiconductors, which narrow the band gap and provide efficient electron flow for hydrogen evolution. In continuation of this, Zhang *et al*. synthesized a noble metal-free RGO–$Zn_{0.8}Cd_{0.2}S$ nanocomposite using convenient co-precipitation–hydrothermal reduction method, for hydrogen evolution [140]. Large surface area, high electrical conductivity and high mobility of charges due to sp^2 hybridization make graphene sheets as a superior material for the immobilization of $Zn_{0.8}Cd_{0.2}S$ nanoparticles. Graphene sheets act as a good electron acceptor for the photogenerated electrons, transferred from the conduction band of $Zn_{0.8}Cd_{0.2}S$, and prevent

the recombination of electrons and holes on the interface of the semiconductor. The synthesized rGO–$Zn_{0.8}Cd_{0.2}S$ nanocomposite showed high H_2 formation rate, i.e., 1824 μmol g^{-1} h^{-1} with optimum rGO content of 0.25 wt.% along with the high apparent quantum efficiency of 23.4% at 420 nm. Moreover, it showed better photocatalytic properties and high quantum efficiency in comparison to $Zn_{0.8}Cd_{0.2}S$ nanoparticles and Pt–$Zn_{0.8}Cd_{0.2}S$ nanocomposites. This study, clearly demonstrated the pivotal role played by rGO in the synthesis of metal free photocatalysts for hydrogen evolution.

RGO–$ZnIn_2S_4$ composite photocatalyst has been evaluated for the visible-light-assisted hydrogen evolution [141]. For the synthesis of the nanocomposite, the precursors of $ZnIn_2S_4$ were deposited on graphene sheets by "*in situ* controlled growth" solvothermal process. TEM analysis showed that very thin layers of $ZnIn_2S_4$ were deposited on RGO, which provided higher surface and active sites. The BET surface area of the synthesized RGO–$ZnIn_2S_4$ composite was found to be much higher (92 m^2 g^{-1}) than pure $ZnIn_2S_4$ (35 m^2 g^{-1}) which clearly emphasize the reason of its enhanced catalytic activity. The optimum concentration of photocatalyst was investigated by varying the amount of photocatalyst, and it was found that 0.05g of catalyst gave optimum hydrogen production rate (81.6 μmol h^{-1}). Further addition of catalyst was detrimental for the process because of shielding of visible irradiation available to other catalytic sites. In another study, Yang *et al*. demonstrated that in case of hybrid GO/SiC photocatalyst containing 1 wt.% of GO, the hydrogen production rate of 95 μL h^{-1} can be achieved in the presence of KI as a sacrificial donor [142].

In general, the enhanced photocatalytic performance of graphene/semiconductor composites is believed to be due to the better charge transportation on its surface, which hampers electron–hole recombination on the semiconductor. Apart from this, a report by Zhang *et al*. suggested that graphene not only provides higher mobility but also works as a macromolecular photosensitizer which helps in the narrowing the band gap of the semiconductor [143]. They synthesized nanosized ZnS on the surface of RGO by a two-step method. ZnS because of its high band gap was unable to generate electron–hole pairs under visible-light irradiation. However, after addition of 5 wt.% graphene, the composite was able to generate electron–hole pairs. Controlled experiments by using hole scavenger *tert*-butyl alcohol (TBA) and ESR studies clearly depicted that graphene (GR) worked as a macromolecular photosensitizer, which provided necessary electrons for photoreaction.

The photocatalytic performance of homogeneous metal complexes immobilized on graphene support was found to be increased mainly due to better charge separation on the surface of graphene. Homogeneous metal complexes work as photosensitizers and can transfer photoexcited electrons

to graphene sheets. It is worthy to mention that neither metal complex photosensitizers nor graphene sheets can promote hydrogen evolution reaction. However, they need an active catalytic site, which can capture and transfer electron to protons. In most cases, Pt metal has been used as an active center for the hydrogen evolution reaction. It has been found that manganese phthalocyanine covalently immobilized on graphene by 1,3-cyloaddition reaction of *N*-methyl glycine and 4-hydroxy benzaldehyde provided better water splitting than MnPc alone [144]. After 10 h visible-light irradiation, the hydrogen formation rate was determined to be 1.45 μmol mg^{-1} with an apparent quantum yield (AQY) of 0.06% in the presence of Pt as a co-catalyst and triethylamine as a sacrificial donor. In another report, Wang *et al*. synthesized covalently immobilized silicon phthalocyanine to nitrogen doped ultra-small-reduced graphene oxide (*N*-usRGO) for the visible-light-assisted hydrogen evolution [145]. The rate of H_2 production by using *N*-usRGO/SiPc as photocatalyst loaded with 5 wt.% Pt as a co-catalyst and triethylamine as a sacrificial donor was 4.5 μmol mg^{-1} after 6 h. The position of LUMO and HOMO of SiPc was –3.75 eV (*vs* vacuum) and –6.18 eV (*vs* vacuum) higher than the conduction band of *N*-usRGO, so electrons can flow easily from SiPc to *N*-usRGO. Furthermore, the lower work function of Pt facilitates electron capturing from *N*-usRGO to prevent back electron transfer and thus enhances the yield of product.

9.6 Metal Free Dye-graphene Composite

Organic metal free dyes are becoming a choice of selection over noble metal-based dyes because of their degradability and nontoxic nature. By choosing suitable dye, the desired spectrum of solar light can be harvested. Moving forward in this direction, Min *et al*. synthesized Eosin Y (EY) dye sensitized RGO loaded with Pt nanoparticles [146]. The developed dye sensitized photocatalyst displayed higher catalytic activity for hydrogen evolution by using triethanolamine as a sacrificial donor. The rate of hydrogen evolution was 14.14 μmol h^{-1} (420 nm) in the first 24 h with AQY of 9.3% under 300-W tungsten halogen lamp. To investigate the effect of Pt and graphene, blank experiments using EY-RGO and EY-Pt were carried out. In the absence of Pt using EY-RGO a very small amount of H_2 (0.18 μmol) was obtained after 22 h, whereas for EY-Pt system in the absence of RGO the hydrogen evolution rate was 0.18 μmol h^{-1}. Addition of small amount of RGO (3 mg), the photocatalytic activity of the EYRGO/Pt system was significantly increased and afforded 10.17 μmol h^{-1}. The mechanism of enhanced activity can be explained on the basis of work function. The work functions of EY and EY*

vs vacuum are about –5.60 and –3.45 eV, respectively [147] and the work function of graphene is –4.66 eV [148] so a large energy band offset will form between EY* and RGO and the excited electrons will transfer from EY to RGO. In a similar study, Mou *et al.* found that EY/RGO/Pt in the weight ratio of 1.0/1.0/0.1 yielded 3350 μmol g^{-1} h^{-1} of H_2 in the presence of triethanolamine under UV–Vis light of 150-W Xenon lamp [149]. The contradictory yield of H_2 in both studies may be due to the use of different light sources. In another study, Min *et al.* used Rose Bengal (RB) dye for the sensitization of RGO loaded with Pt co-catalyst [150]. The RB/RGO/Pt photocatalyst showed a hydrogen production rate of 14.2 μmol g^{-1} h^{-1} with the AQY of 18.5% under 550 nm light irradiation when Pt loading was 6 wt.%.

The whole solar spectrum can be harvested by sensitization of graphene sheets with more than one dye. In this context, Min *et al.* developed a novel dye sensitized catalytic system for hydrogen evolution [151]. They synthesized Pt nanoparticles highly dispersed on RGO with co-sensitization with EY and RB dyes. The presence of organic dyes EY and RB enhanced the visible-light absorption efficiency of the hybrid material. The graphene sheets played a pivotal role in fast and efficient electron transfer on its surface, which minimizes the charge recombination process in dye molecule. Pt worked as electron capturing agent and provided active sites for hydrogen evolution. Blank experiments using RGO were performed with and without Pt in absence of EY and RB dyes; no H_2 was evolved, which confirmed the need for sensitization of graphene sheets. After the absorption of visible light, the electrons from the HOMO orbital move to the LUMO orbital of both dyes, EY and RB, and then transferred to graphene sheets. Graphene sheets provided a conductive electron transport of photogenerated electrons trapped from both dyes to Pt nanoparticles where the hydrogen evolution took place. Triethanolamine worked as a sacrificial donor, facilitating the back reduction of dye molecules to its native state. A high yield of 330 μmol g^{-1} of H_2 after 10 h irradiation with a quantum yield of 37 % was obtained.

9.7 Polymeric Semiconductors/Graphene Composite

Very recently, polymeric semiconductors have emerged as attractive materials in the viewpoint of their polymer type properties along with ability of photocatalysis. Moreover, their band gap can be tailored by chemical modification. Among various polymeric photocatalysts, graphitic carbon nitride (g-C_3N_4) is the most promising due to its low band gap (2.7 eV) and suitable position of conduction band (–1.1 eV) and valence band (+1.6 eV) required for proton or CO_2 reduction and water oxidation, respectively [152]. The g-C_3N_4 is a 2D polymer consisting of interconnected tri-*s*-triazines units *via* tertiary

amines. Many photocatalytic systems have been developed by hybridization of carbon nitride with various semiconductors like $BiVO_4$ [153], TiO_2 [154], WO_3 [155], $NaNbO_3$ [156], Cu_2O [157], CdS [158], Ag_3PO_4 [159], Bi_2WO_6 [160], etc. for various applications including hydrogen evolution and CO_2 reduction. Quantum efficiency for H_2 evolution and CO_2 reduction by carbon nitride can be further increased by dye sensitization like magnesium phthalocyanine, EY, etc. [161]. Ruthenium complex immobilized on carbon nitride by phosphate groups has been shown to enhance the rate of CO_2 reduction to CO [162]. Xiang *et al.* reported g-C_3N_4 modified with RGO (1% graphene/g-C_3N_4 nanohybrid) to be promising catalyst for H_2 production at the rate of 451 μmol g^{-1} h^{-1} in the presence of Pt and methanol [163]. The addition of 1 wt.% RGO increased the methanol yield three times than pure g-C_3N_4 due to the better transportation of charge from the point of generation followed by capturing with Pt nanoparticles.

Another example of polymeric material that can work as photocatalytic material is polyaniline abbreviated as PANI. Jing *et al.* developed a PANI–GR–TiO_2 as a ternary hybrid through a stepwise synthetic route [164]. Firstly, binary GR–TiO_2 was prepared with the attachment of GO on APTMS functionalized TiO_2 followed by hydrothermal reduction than polyaniline was grafted by polymerization in acidic solution. The calculated band gaps of TiO_2, binary GR–TiO_2, and ternary PANI–GR–TiO_2 were 3.23, 2.65, and 2.18 eV, respectively. The developed ternary PANI–GR–TiO_2 hybrid showed enhanced photo-electrochemical performance for the water oxidation reaction. In the proposed mechanism, it has been suggested that HOMO and LUMO of PANI together with graphene may create a favorable p–n heterojunction so electrons from LUMO of excited PANI can move to conduction band of TiO_2 while holes in the valence band of TiO_2 can move to HOMO of PANI.

9.8 Solar Fuel Production by Doped Graphene

Doping with heteroatoms like N [165], S [166], B [167], P [168], etc. can transform conductive graphene to semiconductor, for instance nitrogen-doped graphene possesses a band gap [169]. In general, nitrogen-doped graphene contains three types of nitrogen: pyridinic, quaternary nitrogen, and pyrrolic depending upon their position on the sheets. Only pyridinic nitrogen contributes with their lone pairs to the conjugated π network of graphene. Due to these electrons, the electron rich character of sheets is increased and the Fermi level shifts above the Dirac point, which distorts symmetry of graphene sub-lattice and creates a band gap [170]. The value of the created band gap depends strongly on the N/C ratio in the sheets and

a band gap up to 5 eV can be reached [171]. The appropriate N/C ratio can be obtained by using different nitrogen sources. Two main strategies, *i.e.,* direct synthesis and post treatment strategy were used for the synthesis of N-doped graphene. In the direct synthesis method, GO was reduced in the presence of nitrogen containing substance like ethylene diamine, carbon nitride, hydrazine hydrate, urea, NH_3, etc. In the direct synthesis, higher N/C ratio and even distribution can be obtained. In the post-treatment strategy, RGO was doped with nitrogen by N_2 gas, NH_3, or plasma synthesis method. The intensity ratio of N1s peak at binding energy 400 eV and C1s peak at 284 eV in XPS spectra is used for determining the nitrogen content along with the types of nitrogen present [172]. Furthermore, due to the nitrogen doping, the charge distribution on neighboring atoms are disturbed and negative charge is accumulated on the surface of graphene, creating "activation regions" on the graphene sheet. These activation regions can be utilized for oxygen reduction reactions as well as for attachment of metal particles/semiconductors/metal complexes, etc. Several nanocomposites of N-doped graphene/semiconductor have been synthesized in order to enhance the photocatalytic performance like oxygen and hydrogen evolution reactions. For instance, N-doped graphene/CdS composite exhibited higher photocatalytic performance for hydrogen generation than graphene/CdS composite [173].

Moreover, the electron rich character of N-doped graphene sheets can be utilized for the attachment of positively charged metal complexes, which can improve the absorption capacity in the visible region. In this regards Kumar *et al.* synthesized N-doped graphene immobilized $[Cu(bpy)_2(H_2O)_2]Cl_2.2H_2O$ nanohybrid photocatalyst (GrN_{700}–CuC) for the reduction of CO_2 to methanol [174]. N-doped graphene having 6.01% N was synthesized by reducing followed by annealing of GO in the presence of ethylenediamine as nitrogenous source. Then copper complex was immobilized to N-doped graphene by targeting lone pairs of electrons. The catalyst exhibited enhanced photoactivity toward reduction of CO_2 to methanol due to continuous pumping of electrons from photoexcited copper complex. The methanol production rate was 66.6 μmol g^{-1} h^{-1} (quantum yield 0.021) after 24 h with 0.77 μmol g^{-1} h^{-1} (quantum yield 5.8×10^{-4}) of hydrogen as byproduct under 20 W LED as visible-light source. It was assumed that DMF works as a hole scavenger in this process.

Likewise, N-doped graphene P-doped graphene, due to presence of phosphorous heteroatom contributes electrons in π-networks, and behaves as a semiconductor. P-doped graphene can be synthesized by the reduction of GO in the presence of phosphorus source like phosphoric acid, or P-containing ionic liquids, etc. [175]. In contrast to these methods, Sanchez

et al. synthesized P-doped graphene nanosheets by pyrolysis of $H_2PO_4^-$ modified alginate at 900 °C under inert atmosphere [176]. The P-doped graphene produced with alginate having higher phosphate proportion, (PG-4), has higher C [%]/P [%] ratio that was 12.73 and optical band gap (2.85 eV) as obtained by onset of UV–Vis spectra. Furthermore, it has been elucidated that the increased P content increases the amount of hydrogen evolved. In the presence of Pt co-catalyst and triethanolamine sacrificial donor, a hydrogen evolution rate of 282 μmol g^{-1} h^{-1} was obtained.

9.9 Conclusion

In this chapter, we have attempted to review the recent trends in the field of production of solar fuels *via* water splitting and CO_2 reduction using graphene-semiconductor-based nanocomposite/hybrid materials as photoredox catalysts. Graphene/semiconductor hybrids served as better photocatalysts in comparison to semiconductors due to the synergistic effect of both components for better mobility of electrons on its surface as well enhancing visible-light absorption range of the semiconductor. Band gap creation by oxidation of graphene to graphene oxide and doping with heteroatoms is an important approach for harvesting solar radiation on a partially conductive surface, which can provide better charge separation. Furthermore, immobilization of metal complexes on GO or doped-graphene sheets has proven to display enhanced catalytic performance due to better charge injection in the conduction band of semiconductive GO and doped-graphene sheets. The role of graphene in the graphene/semiconductor surface was not limited up to providing better charge separation due to quantum confinement effect, but graphene can serve as macromolecular photosensitizer. At this stage, it can be concluded from the recent past that graphene is a "rising star", which can help to solve the problems of energy crisis and global warming.

References

1. R. K. de Richter, T. Ming and S. Caillol, *Renew. Sustain. Energy Rev*., 19, 82–106, 2013.
2. M. Tahir and N.A.S. Amin, *Renew. Sustain. Energy Rev*., 25, 560–579, 2013.
3. V. P. Indrakanti, J. D. Kubicki and H. H. Schobert, *Energy Environ. Sci*., 2, 745–758, 2009.
4. M. M. Halmann and M. Steinberg, *Greenhouse Gas Carbon Dioxide Mitigation Science and Technology*, Lewis Publishers, 1999.

5. H. Yang, Z. Xu, M. Fan, R. Gupta, R. B. Slimane, A. E. Bland and I. Wright, *J. Environ. Sci.*, 20, 14, 2008.
6. R. E. Morris and P. S. Wheatley, *Angew. Chem., Int. Ed*., 47, 4966, 2008.
7. Y. Wang, K. S. Chen, J. Mishler, S. C. Cho and X. C. Adroher, *Appl. Energy,* 88, 981–1007, 2011.
8. http://www.esrl.noaa.gov/gmd/ccgg/trends/weekly.html
9. D.T. Reindl, W.A. Beckman and J.A. Duffie, *Solar Energy*, 45, 9–17, 1990.
10. M. Aresta and A. Dibenedetto, *Dalton Trans*., 2975, 2007.
11. M. Aresta, *Carbon Dioxide Reduction and Use as a Chemical Feedstock,* W. B. Tolman, Ed.; Wiley-VCH: Weinheim, Germany, 1–41, 2006.
12. A. Listorti, J. Durrant and J. Barber, *Nature Mater*., 8, 929, 2009.
13. D. Kim, K. Sakimoto, D. Hong and P. Yang, *Angew. Chem., Int. Ed*., 54, 3259, 2015.
14. H. Li, Y. Zhou, W. Tu, J. Ye and Z. Zou, *Adv. Funct. Mater*, 25, 998, 2015.
15. G. A. Olah, *Angew. Chem., Int. Ed.,* 52, 104–107, 2013.
16. E. E. Benson, C. P. Kubiak, A. J. Sathruma and J. M. Smiejaa, *Chem. Soc. Rev*., 38, 89–99, 2009.
17. A. L. Linsebigler, G. Lu and J. T. Yates, *Chem. Rev.,* 95, 735–758, 1995.
18. S. C. Roy, O. K. Varghese, M. Paulose and C. A. Grimes, *ACS Nano*, 4, 1259–1278, 2010.
19. T. Inoue, A. Fujishima, S. Konishi and K. Honda, *Nature*, 277, 637–638, 1979.
20. H.-Y. Li, J. Wu, X.-H. Zhou, L.-C. Kang, D.-P. Li, Y. Sui, Y.-H. Zhou, Y.-X. Zheng, J.-L. Zuo and X.-Z. You, *Dalton Trans*., 10563–10569, 2009.
21. A. J. Morris, G. J. Meyer and E. Fujita, *Acc. Chem. Res.,* 12, 1983–1994, 2009.
22. J. Michl, *Nature Chem.,* 3, 268–269, 2011.
23. X.-T. Zhou, H.-B. Ji and X.-J. Huang, *Molecules*, 17, 1149–1158, 2012.
24. Z. Zhao, J. Fan, M. Xie and Z. Wang, *J. Cleaner Prod.,* 17, 1025–1029, 2009.
25. Z. Wang, W. Mao, H. Chen, F. Zhang, X. Fan and G. Qian, *Catal. Commun.,* 7, 518–522, 2006.
26. M. R. Hoffmann, J. A. Moss and M. M. Baum, *Dalton Trans*., 40, 5151–5158, 2011.
27. A. Fujishima and K. Honda, *Nature*, 44, 1148–1150, 1971.
28. T. Inoue, A. Fujishima, S. Konishi and K. Honda, *Nature,* 277, 637–638, 1979.
29. Y. Izumi, *Coord. Chem. Rev*., 257, 171–186, 2013.
30. S. Sato, T. Arai and T. Morikawa, *Inorg. Chem.*, 54, 5105–5113, 2015.
31. K. Nagaveni, M. S. Hegde, N. Ravishankar, G. N. Subbanna and G. Madras, *Langmuir*, 20, 2900–2907, 2004.
32. S. G. Kumar and L. G. Devi, *J. Phys. Chem. A*, 115, 13211–13241, 2011.
33. K. Hashimoto, H. Irie and A. Fujishima, *Jpn. J. Appl. Phys.*, 44, 8269–8285, 2005.
34. S. N. Habisreutinger, L. S.-Mende and J. K. Stolarczyk, *Angew. Chem. Int. Ed*., 52, 7372–7408, 2013.

35. A. Naldoni, M. Allieta, S. Santangelo, M. Marelli, F. Fabbri, S. Cappelli, C. L. Bianchi, R. Psaro and V. D. Santo, *J. Am. Chem. Soc.*, 134, 7600–7603, 2012.
36. S. U. M. Khan, M. Al-Shahry and W.B. Ingler Jr., *Science*, 297, 2243–2245, 2002.
37. J. H. Park, S. Kim and A. J. Bard, *Nano Lett.*, 6, 24–28, 2006.
38. D. Chen, Z. Jiang, J. Geng, Q. Wang and D. Yang, *Ind. Eng. Chem. Res.*, 46, 2741–2746, 2007.
39. X. Li, Z. Zhuang, W. Li and H. Pan, *Appl. Catal. A*, 429– 430, 31–38, 2012.
40. R. Asahi, T. Morikawa, T. Ohwaki, K. Aoki and Y. Taga, *Science*, 293, 269–271, 2001.
41. Q. W. Zhang, J. Wang, S. Yin, T. Sato and F. Saito, *J. Am. Chem. Soc.* 126, 1161–1163, 2004.
42. W. Balcerski, S. Y. Ryu and M. R. Hoffmann, *J. Phys. Chem. C*, 111, 15357–15362, 2007.
43. J. Wang, D. N. Tafen, J. P. Lewis, Z. Hong, A. Manivannan, M. Zhi, M. Li and N. Wu, *J. Am. Chem. Soc.*, 131, 12290–12297, 2009.
44. M. Tahir and N. S. Amin, *Energy Convers. Manage.*, 76, 194–214, 2013.
45. Q. Xiang, J. Yu, W. Wang and M. Jaroniec, *Chem. Commun.*, 47, 6906–6908, 2011.
46. G. Liu, C. Sun, H. G. Yang, S. C. Smith, L. Wang, G. Q. Lu and H.-M. Cheng, *Chem. Commun.*, 46, 755–757, 2010.
47. X. Wu, Z. Chen, G. Q. Lu, and L. Wang, *Adv. Funct. Mater.*, 21, 4167–4172, 2011.
48. M. A. Barakat, H. Schaeffer, G. Hayes and S. Ismat-Shah, *Appl. Catal. B*, 57, 23–30, 2005.
49. Y. Lu, Y. Lin, D. Wang, L. Wang, T. Xie and T. Jiang, *Nano Res.*, 4, 1144–1152, 2011.
50. K. Lalitha, G. Sadanandam, V. D. Kumari, M. Subrahmanyam, B. Sreedhar and N. Y. Hebalkar, *J. Phys. Chem. C*, 114, 22181–22189, 2010.
51. N. Sasirekha, S. J. S. Basha and K. Shanthi, *Appl. Catal. B*, 62, 169–180, 2006.
52. T. Ohno, F. Tanigawa, K. Fujihara, S. Izumi and M. Matsumura, *J. Photochem. Photobiol. A*, 127, 107–110, 1999.
53. J. Yu and J. Ran, *Energy Environ. Sci.*, 4, 1364–1371, 2011.
54. S. Liu, E. Guo and L. Yin, *J. Mater. Chem.,* 22, 5031–5041, 2012.
55. G. Colón, M. Maicu, M.C. Hidalgo and J. A. Navío, *Appl. Catal. B*, 67, 41–51, 2006.
56. H. Li, Z. Bian, J. Zhu, Y. Huo, H. Li and Y. Lu, *J. Am. Chem. Soc.*, 129, 4538–4539, 2007.
57. R. S. Sonawane and M. K. Dongare, *J. Mol. Catal. A*, 243, 68–76, 2006.
58. B. H. Meekins and P. V. Kamat, *J. Phys. Chem. Lett.*, 2, 2304–2310, 2011.
59. A. Yamakata, T.-aki Ishibashi and H. Onishi, *J. Phys. Chem. B*, 106, 9122–9125, 2002.
60. I. Paramasivam, H. Jha, N. Liu and P. Schmuki, *Small*, 8, 3073–3103, 2012.

61. T. W. Woolerton, S. Sheard, E. Reisner, E. Pierce, S. W. Ragsdale and F. A. Armstrong, *J. Am. Chem. Soc*., 132, 2132, 2010.
62. S. O. Obare, T. Ito and G. J. Meyer, *J. Am. Chem. Soc*., 128, 712–713, 2006.
63. X. Li, Q. Wang, Y. Zhao, W. Wu, J. Chen and H. Meng, *J. Colloid Interface Sci.,* 411, 69–75, 2013.
64. A. Mclaren, T. V.-Solis, G. Li and S. C. Tsang, *J. Am. Chem. Soc*., 131, 12540–12541, 2009.
65. X. Lu, G. Wang, S. Xie, J. Shi, W. Li, Y. Tong and Y. Li, *Chem. Commun*., 48, 7717–7719, 2012.
66. P. Johne and H. Kisch, *J. Photochem. Photobiol. A,* 111, 223–228, 1997.
67. Z.-Y. Wang, H.-C. Chou, J. C. S. Wu, D. P. Tsai and G. Mul, *Appl. Catal. A*, 380, 172–177, 2010.
68. S. C. Yan, S. X. Ouyang, J. Gao, M. Yang, J. Y. Feng, X. X. Fan, L. J. Wan, Z. S. Li, J. H. Ye, Y. Zhou and Z. G. Zou, *Angew. Chem. Int. Ed.*, 49, 6400–6404, 2010.
69. H. Kisch and P. Lutz, *Photochem. Photobiol. Sci*., 1, 240–245, 2002.
70. P. Praus, O. Kozak, K. Koci, A. Panacek and R. Dvorsky, *J. Colloid Interface Sci*., 360, 574–579, 2011.
71. H.-Y. Lin, Y.-F. Chen and Y.-W. Chen, *Int. J. Hydrogen Energy*, 32, 86–92, 2007.
72. Y. P. Xie, G. Liu, L. Yin and H.-M. Cheng, *J. Mater. Chem.* 22, 6746–6751, 2012.
73. B. Borresen, G. Hagen and R. Tunold, *Electrochim. Acta*, 47, 1819–1827, 2002.
74. K. Maeda, K. Teramura, D. Lu, T. Takata, N. Saito, Y. Inoue and K. Domen, *J. Phys. Chem. B*, 110, 13753–13758, 2006.
75. T. Kodama, N. Gokon and Yamamoto, *Solar Energy*, 82, 73–79, 2008.
76. M. Moriya, T. Minegishi, H. Kumagai, M. Katayama, J. Kubota and K. Domen, *J. Am. Chem. Soc.*, 135, 3733–3735, 2013.
77. K. Maeda, M. Higashi, D. Lu, R. Abe and K. Domen, *J. Am. Chem. Soc*., 132, 5858–5868, 2010.
78. Q. Jia, A. Iwasea and A. Kudo, *Chem. Sci.,* 5, 1513–1519, 2014.
79. R. Abe, K. Sayama and H. Sugihara, *J. Phys. Chem. B,* 109, 16052–16061, 2005.
80. M. Higashi, R. Abe, A. Ishikawa, T. Takata, B. Ohtani and K. Domen, *Chem. Lett.,* 37, 138–139, 2008.
81. R. Konta, T. Ishii, H. Kato and A. Kudo, *J. Phys. Chem. B,* 108, 8992, 2004.
82. A. J. Cowan and J. R. Durrant, *Chem. Soc. Rev.,* 42, 2281–2293, 2013.
83. P. Kumar, R. K. Chauhan, B. Sain and S. L. Jain, *Dalton Trans.*, 44, 4546–4553, 2015.
84. T. Nyokong, *Coord. Chem. Rev.*, 251, 1707–1722, 2007.
85. P. Kumar, C. Joshi, N. Labhsetwar, R. Boukherroub and S. L. Jain, *Nanoscale*, 7, 15258–15267, 2015.
86. A. K. Geim and K. S. Novoselov, *Nat. Mater.* 6, 183–191, 2007.

87. D. R. Dreyer, R. S. Ruoff and C. W. Bielawski, *Angew. Chem., Int. Ed*., 49, 9336–9344, 2010.
88. N. Zhang, Y. Zhang and Y.-J. Xu, *Nanoscale*, 4, 5792–5813, 2012.
89. Q. Xiang, J. Yu and M. Jaroniec, *Chem. Soc. Rev*., 41, 782–796, 2012.
90. L. P. Biro, P. N.-Incze and P. Lambin, *Nanoscale*, 4, 1824–1839, 2012.
91. M. R. Das, P. Sharma, S. C. Borah, S. Szunerits and R. Boukherroub, *Innovative Graphene Technologies: Developments and Characterization;* A. Tiwari, Rapra Publishers, USA, 2013.
92. Q. Xiang, B. Cheng and J. Yu, *Angew. Chem. Int. Ed.* 54, 11350–11366, 2015.
93. Y. Shao, J. Wang, H. Wu, J. Li*u,* I. A. Aksay and Y. Lin, *Electroanalysis*, 22, 1027–1036, 2010.
94. M. D. Stoller, S. Park, Y. Zhu, J. An and R. S. Ruoff, *Nano Lett.*, 8, 3498–3502, 2008.
95. T.-F. Yeh, J. Cihlar, C.-Y. Chang, C. Cheng and H. Teng, *Mater. Today*, 16, 78–84, 2013.
96. B. F. Machado and P. Serp, *Catal. Sci. Technol.*, 2, 54–75, 2012.
97. Q. Xiang and J. Yu, *J. Phys. Chem. Lett.*, 4, 753–759, 2013.
98. Y. C. Qiu, K. Y. Yan, S. H. Yang, L. M. Jin, H. Deng and W. S. Li, *ACS Nano*, 4, 6515, 2010.
99. T. G. Xu, L. W. Zhang, H. Y. Cheng and Y. F. Zhu, *Appl. Catal. B*, 101, 382, 2011.
100. G. Williams and P. V. Kamat, *Langmuir*, 25, 13869, 2009.
101. J. M. Lee, Y. B. Pyun, J. Yi, J. W. Choung and W. I. Park, *J. Phys. Chem. C,* 113, 19134, 2009.
102. P.-Q. Wang, Y. Bai, P.-Y. Luo and J.-Y. Liu, *Cat. Commun.,* 38, 82–85, 2013.
103. C. Xu, X. Wang and J. W. Zhu, *J. Phys. Chem. C*, 112, 19841, 2008.
104. K. Morishige and T. Hamada, *Langmuir*, 21, 6277, 2005.
105. J. Yan, Z. J. Fan, T. Wei, W. Z. Qian, M. L. Zhang and F. Wei, *Carbon,* 48, 3825, 2010.
106. D. Du, J. Liu, X. Y. Zhang, X. L. Cui and Y. H. Lin, *J. Mater. Chem.,* 21, 8032, 2011.
107. C. Nethravathi, T. Nisha, N. Ravishankar, C. Shivakumara and M. Rajamathi, *Carbon,* 47, 2054, 2009.
108. A. N. Cao, Z. Liu, S. S. Chu, M. H. Wu, Z. M. Ye, Z. W. Cai, Y. L. Chang, S. F. Wang, Q. H. Gong and Y. F. Liu, *Adv. Mater.,* 22, 103, 2010.
109. X. M. Geng, L. Niu, Z. Y. Xing, R. S. Song, G. T. Liu, M. T. Sun, G. S. Cheng, H. J. Zhong, Z. H. Liu, Z. J. Zhang, L. F. Sun, H. X. Xu, L. Lu and L. W. Liu, *Adv. Mater.*, 22, 638, 2010.
110. E. P. Gao, W. Z. Wang, M. Shang and J. H. Xu, *Phys. Chem. Chem. Phys.,* 13, 2887, 2011.
111. Y. H. Ng, A. Iwase, A. Kudo and R. Amal, *J. Phys. Chem. Lett.,* 1, 2607, 2010.
112. A. Mukherji, B. Seger, G. Q. Lu and L. Wang, *ACS Nano*, 5, 3483–3492, 2011.

113. X. Lin, Y. Wang, J. Zheng, C. Liu, Y. Yang and G. Che, *Dalton Trans*., 44, 19185–19193, 2015.
114. Y. S. Fu and X. Wang, *Ind. Eng. Chem. Res.*, 50, 7210, 2011.
115. K. P. Loh, Q. Bao, G. Eda and M. Chhowalla, *Nat. Chem.*, 2, 1015–1024, 2010.
116. G. Eda, C. Mattevi, H. Yamaguchi, H. Kim and M. Chhowalla, *J. Phys. Chem. C,* 113, 15768–15771, 2009.
117. H. C. Hsu, I. Shown, H. Y. Wei, Y. C. Chang, H. Y. Du, Y. G. Lin, C. A. Tseng, C. H. Wang, L. C. Chen, Y. C. Lin and K. H. Chen, *Nanoscale*, 5, 262–268, 2013.
118. T.-F. Yeh, J.-M. Syu, C. Cheng, T.-H. Chang and H. Teng, *Adv. Funct. Mater*., 20, 2255–2262, 2010.
119. I. Shown, H.-C. Hsu, Y.-C. Chang, C.-H. Lin, P. K. Roy, A. Ganguly, C.-H. Wang, J.-K. Chang, C.-I. Wu, L.-C. Chen and K.-H. Chen, *Nano Lett.*, 14, 6097–6103, 2014.
120. X. Xu, T. Lu, X. Liu and X. Wang, *Chem. Eur. J.,* 21, 14638–14647, 2015.
121. K. Yang, Y. Dai and B. Huang, *J. Phys. Chem. C*, 111, 12086–12090, 2007.
122. F. Pei, Y. Liu, S. Xu, J. Lu, C. Wang and S. Cao, *Int. J. Hydrogen Energy*, 38, 2670–2677, 2013.
123. L. -L. Tan, W.-J. Ong, S. P. Chai, B. T. Goh and A. R. Mohamed, *Appl. Catal. B.,* 179, 160–170, 2015.
124. L.-L. Tan, W.-J. Ong, S.-P. Chai and A. R. Mohamed, *Chem. Commun.,* 50, 6923–6926, 2014.
125. L. Liu, C. Zhao, D. Pitts, H. Zhao and Y. Li, *Catal. Sci. Technol*. 4, 1539–1546, 2014.
126. W.-N. Wang, W.-J. An, B. Ramalingam, S. Mukherjee, D. M. Niedzwiedzki, S. Gangopadhyay and P. Biswas, *J. Am. Chem. Soc*. 134, 11276–11281, 2012.
127. S. Kumar, P. Kumar and S. L. Jain, *J. Mater. Chem. A*, 2, 18861–18866, 2014.
128. Y. Yu, M. Zhou, W. Shen, H. Zhang, Q. Cao and H. Cui, *Carbon*, 50, 2539–2545, 2012.
129. P. Kumar, B. Sain and S. L. Jain, *J. Mater. Chem. A,* 2, 11246–11253, 2014.
130. P. Kumar, A. Kumar, B. Sreedhar, B. Sain, S. S. Ray and S. L. Jain, *Chem. Eur. J.,* 20, 6154–6161, 2014.
131. P. Kumar, A. Bansiwal, N. Labhsetwar and S. L. Jain, *Green Chem.*, 17, 1605–1609, 2015.
132. P. Kumar, N. G. Naumov, R. Boukherroub and S. L. Jain, *Appl. Catal. A*, 499, 32–38, 2015.
133. P. Kumar, H. P. Mungse, S. Cordier, R. Boukherroub, O. P. Khatri, S. L. Jain, *Carbon*, 94, 91–100, 2015.
134. R. Gusain, P. Kumar, O. P. Sharma, S. L. Jain and O. P. Khatri, *Appl. Catal. B*, 181, 352–362, 2016.
135. L. Zhang, N. Li, H. Jiu, G. Qi and Y. Huang, *Ceramic Int.*, 41, 6256–6262, 2015.
136. Y. Li, H. Wang, L. Xie, Y. Liang, G. Hong and H. Dai, *J. Am. Chem. Soc.* 133, 7296–7299, 2011.

137. Q. Xiang, J. Yu and M Jaroniec, *J. Am. Chem. Soc.* 134, 6575–6578, 2012.
138. Z. Khan, T. R. Chetia, A. K. Vardhaman, D. Barpuzary, C. V. Sastri and M. Qureshi, *RSC Adv.,* 2, 12122–12128, 2012.
139. L.-L. Tan, W.-J. Ong, S.-P. Chai, A. R. Mohamed, *Appl. Catal. B.,* 2015, 166–167, 251–259.
140. J. Zhang, J. Yu, M. Jaroniec and J. R. Gong, *Nano Lett.* 12, 4584–4589, 2012.
141. J. Zhou, G. Tian, Y. Chen, X. Meng, Y. Shi, X. Cao, K. Pan and H. Fu, *Chem. Commun.,* 49, 2237–2239, 2013.
142. J. Yang, X. Zeng, L. Chen and W. Yuan, *Appl. Phys. Lett.* 102, 083101, 2013.
143. Y. Zhang, N. Zhang, Z.-R. Tang and Y.-J. Xu, *ACS Nano*, 6, 9777–9789, 2012.
144. D. Wang, J. Huang, X. Li, P. Yang, Y. Du, C. M Goh and C. Lu, *J. Mater. Chem.*, 3, 4195–4202, 2015.
145. J. Huang, Y. Wu, D. Wang, Y. Ma, Z. Yue, Y. Lu, M. Zhang, Z. Zhang and P. Yang, *ACS Appl. Mater. Interfaces*, 7, 3732–3741, 2015.
146. S. Min and G. Lu, *J. Phys. Chem. C*, 115, 13938–13945, 2011.
147. G. D. Sharma, P. Balraju, M. Kumar and M. S. Roy, *Mater. Sci. Eng. B,* 162, 32, 2009.
148. Y. Lin, K. Zhang, W. F. Chen, Y. D. Liu, Z. Y. Geng, J. Zeng, N. Pan, L. F. Yan, X. P. Wang and J. G. Hou, *ACS Nano*, 4, 3033, 2010.
149. Z. Mou, Y. Dong, S. Li, Y. Du, X. Wang, P. Yang and S. Wang, *Int. J. Hydrogen Energy* 36, 8885–8893, 2011.
150. S. Min and G. Lu, *Int. J. Hydrogen Energy*, 38, 2106–2116, 2013.
151. S. Min and G. Lu, *Int. J. Hydrogen Energy*, 37, 10564–10574, 2012.
152. Y. Zheng, J. Liu, J. Liang, M. Jaroniec and S. Z. Qiao, *Energy Environ. Sci.,* 5, 6717–6731, 2012.
153. C. Li, S. Wang, T. Wang, Y. Wei, P. Zhang and J. Gong, *Small,* 10, 2783, 2014.
154. B. Chai, T. Peng, J. Mao, K. Li and L. Zan, *Phys. Chem. Chem. Phys.*, 14, 16745–16752, 2012.
155. Z. Jin, N. Murakami, T. Tsubotan and T. Ohno, *Appl. Catal. B,* 2014, 150–151, 479.
156. G. Li, N. Yang, W. Wang and W. F. Zhang, *J. Phys. Chem. C,* 113, 14829, 2009.
157. J. Chen, S. Shen, P. Guo, M. Wang, P. Wu, X. Wang and L. Guo, *Appl. Catal. B*, 2014, 152–153, 335.
158. J. Zhang, Y. Wang, J. Jin, Z. Lin, F. Huang and J. Yu, *ACS Appl. Mater. Interfaces,* 5, 10317, 2013.
159. S. Kumar, T. Surendar, A. Baruah and V. Shanker, *J. Mater. Chem. A,* 1, 5333, 2013.
160. L. Ge, C. Han and J. Liu, *Appl. Catal. B*, 108–109, 100–107, 2011.
161. K. Takanabe, K. Kamata, X. Wang, M. Antonietti, J. Kubotaa and K. Domen, *Phys. Chem. Chem. Phys.,* 12, 13020–13025, 2010.
162. R. Kuriki, K. Sekizawa, O. Ishitani and K. Maeda, *Angew. Chem. Int. Ed.,* 54, 2406–2409, 2015.
163. Q. Xiang, J. Yu and M. Jaroniec, *J. Phys. Chem. C,* 115, 7355, 2011.

164. L. Jing, Z.-Y. Yang, Y.-F. Zhao, Y.-X. Zhang, X. Guo, Y.-M. Yan and K.-N. Sun, *J. Mater. Chem. A,* 2, 1068–1075, 2014.
165. P. Rani and V. K. Jindal, *RSC Adv*., 3, 802–812, 2013.
166. H. L. Poh, P. Šimek, Z. Sofer and M. Pumera, *ACS Nano*, 7, 5262–5272, 2013.
167. T. B. Martins, R. H. Miwa, Antônio J. R. da Silva, and A. Fazzio, *Phys. Rev. Lett.,* 98, 196803, 2007.
168. R. Li, Z. Wei, X. Gou and W. Xu, *RSC Adv.*, 3, 9978–9984, 2013.
169. M. Deifallah, P. F. McMillan and F. J. Cora, *J. Phys. Chem. C*, 112, 5447–5453, 2008.
170. A. Lherbier, X. Blase, Y. M. Niquet, F. Triozon and S. Roche, *Phys. Rev. Lett*., 101, 036808, 2008.
171. M. Deifallah, P. F. McMillan and F. Cora, *J. Phys. Chem. C*, 112, 5447, 2008.
172. A. L. M. Reddy, A. Srivastava, S. R. Gowda, H. Gullapalli, M. Dubey and P. M. Ajayan, *ACS Nano*, 4, 6337, 2010.
173. L. Jia, D.-H. Wang, Y.-X. Huang, A.-W. Xu and H.-Q. Yu, *J. Phys. Chem. C*, 115, 11466–11473, 2011.
174. P. Kumar, H. P. Mungse, O. P. Khatri and S. L. Jain, *RSC Adv.,* 5, 54929–54935, 2015.
175. Y. Wen, B. Wang, C. Huang, L. Wang and D. H.-Jurcakova, *Chem. Eur. J.,* 21, 80–85, 2015.
176. M. L.-Sanchez, A. Primo and H. Garcia, *Angew. Chem. Int. Ed.*, 52, 11813–11816, 2013.